

See discussions, stats, and author profiles for this publication at: <https://www.researchgate.net/publication/231645888>

UV-Sensitized Generation of Phasepure Cobalt-Doped Anatase: $\text{Co}_x\text{Ti}_{1-x}\text{O}_2$ -delta Nanocrystals with Ferromagnetic Behavior Using Nano- $\text{TiO}_2/\text{cis}[\text{Co-III}(\text{en})_2(\text{MeNH}_2)\text{Cl}](2+)$

ARTICLE in THE JOURNAL OF PHYSICAL CHEMISTRY C · FEBRUARY 2011

Impact Factor: 4.77 · DOI: 10.1021/jp1064227

CITATIONS

13

READS

25

1 AUTHOR:



Krishnamoorthy Anbalagan

Pondicherry University

64 PUBLICATIONS 257 CITATIONS

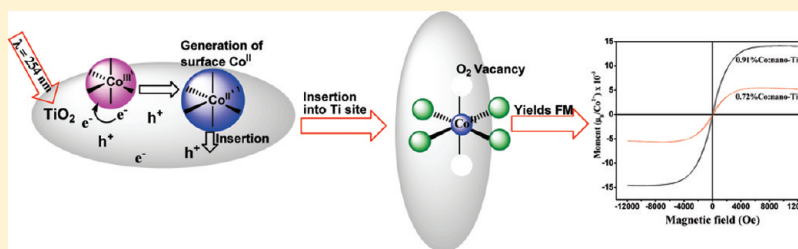
SEE PROFILE

UV-Sensitized Generation of Phasepure Cobalt-Doped Anatase: $\text{Co}_x\text{Ti}_{1-x}\text{O}_{2-\delta}$ Nanocrystals with Ferromagnetic Behavior Using Nano- $\text{TiO}_2/\text{cis}[\text{Co}^{\text{III}}(\text{en})_2(\text{MeNH}_2)\text{Cl}]^{2+}$

K. Anbalagan*

Department of Chemistry, Pondicherry University, Kalapet, Pondicherry 605014, India

ABSTRACT: Anatase nanoparticles, $\text{Co}_x\text{-Ti}_{1-x}\text{O}_{2-\delta}$ (x = dopant density in at % and δ = concentration of oxygen vacancy in the lattice) were synthesized using UV ($\lambda = 254$ nm)-induced photoreduction of surface preadsorbed $\text{cis}[\text{Co}^{\text{III}}(\text{en})_2(\text{MeNH}_2)\text{Cl}]^{2+}$ complex ion on nanoscale TiO_2 particle surfaces in an aqueous solution. Photogenerated dopant, Co^{II} , has successfully implanted in the semiconductor host lattice, preserving anatase crystal phase without the formation of impurity phase like rutile. Such materials termed as diluted magnetic semiconductors (DMSs), if realized without undesirable phases, are projected to have significant implications for the evolving fields of spintronics and advanced magneto-optics. The light dosage was systematically varied to prepare nanostructured semiconductor particles with varying dopant density in the anatase matrix leading to: $x\%, \text{Co}/\text{nano-TiO}_2$; $0.91 \leq x \leq 1.26$ at % nonstoichiometric compound. The compound has been found to show altered optical, compositional, and room-temperature ferromagnetic properties with respect to the undoped TiO_2 nanoparticles. X-ray diffraction measurements showed characteristic anatase reflections and supplied information about the absence of coexisting rutile impurity phase. The nanoparticles are ferromagnetic, having their hysteresis loops in the range -4000 Oe $< H < +4000$ Oe with the specific magnetizations of $(14.40$ to $0.196) \times 10^{-3} \mu_{\text{B}}/\text{Co}^{\text{II}}$ at 300 K. However, the magnetic property depends critically on oxygen vacancy (V^0_{O} , V^+_{O}) and the Co content. A combined study of PL, XRF, SEM-EDX, HRTEM, XPS, and Raman techniques was used to investigate the size, dopant-distribution, composition, and surface structure. Cobalt dopant is predominantly substitutional, $\text{Co}^{\text{II}}_{\text{sub}}$ in anatase lattice and in +2 formal oxidation state. SEM and HRTEM images revealed obvious variations in the surface morphology of raw and Co implanted anatase. This strategy provides an alternative route to synthesize nanosized phase pure anatase $x\%, \text{Co}/\text{nano-TiO}_2$ showing room temperature ferromagnetism, which is expected to open up a general method for the synthesis of other transition-metal-doped nano- TiO_2 .



1. INTRODUCTION

Integrating spin functionality into nonmagnetic materials has become a highly desirable goal in the last years. For instance, dilute magnetic impurities in semiconductors produce materials that are appealing for spintronics.^{1–3} This is a rapidly developing research area in which the electron spin plays an important role in addition to the usual charge degree of freedom. For practical applications, ferromagnetic semiconductors are required to have high Curie temperature (T_c). The possibility of simultaneous control of charge currents and spin polarized currents in those systems might provide new qualities to information processing technologies. Nanoscale diluted magnetic semiconductors (DMS) are the main components of proposed spintronics devices. DMSs are mostly the II–VI or III–V compounds, in which the cations of host lattice are replaced with magnetic impurities up to a few atomic percent. Some of those materials exhibit interesting magnetic and magneto optical behavior characterized³ by a high Curie-temperature ferromagnetism.

Theoretical predictions have identified wide band-gap metal oxide semiconductors (TiO_2 and ZnO) as good candidates for the host materials, which after doping with transition-metal ions could support room-temperature ferromagnetism. Titanium dioxide semiconductor has been extensively investigated for its interesting electrical, optical, electrochemical,⁴ and photocatalytic properties in water⁵ cleavage. It occurs in different crystalline⁶ modifications, rutile (stable phase), anatase (low-temperature phase), monoclinic B-phase ($\text{TiO}_2\text{-B}$), and brookite (metastable phase). Anatase is tetragonal ($I4_1/amd$) composed of stacked tetragonal edge sharing octahedrons formed by six oxygen anions. Anatase crystalline form can function as the most efficient photocatalyst, which is also more desirable than that of the rutile structure. Furthermore, cobalt-doped TiO_2 is promising for the

Received: July 12, 2010

Revised: December 7, 2010

Published: February 22, 2011

spintronics applications^{1,2,7} because of the excellent optical transmission in the visible and near-infrared regions and high *n*-type carrier mobility. Since the discovery of high T_C ferromagnetism in Co^{II}-doped TiO₂ anatase films, there was an expansion of experimental and theoretical work focused on transition-metal-doped TiO₂ as a ferromagnetic material. However, most of the research was confined on thin films, whereas there was significantly less focus on the transition-metal-doped¹ nanoparticles. The paucity of the published research on synthesis of the free-standing high-quality nanoparticles doped with the transition-metal ions is related to a number of challenges such as high surface-to volume ratio, requests for uniform size distribution of the nanocrystals, as well as successful doping, that is, control of exact position of the dopant ions within a crystal.

Nanometer-sized diluted magnetic semiconductors, if realized in homogeneous form without extrinsic undesirable phases, are projected to have significant implications in the evolving fields of spintronics and in advanced magneto-optics. If successfully produced, spintronics devices may offer low power consumption and greater operating speeds than their charge-based analogs and may display new functional properties having no charge-based analog. Such materials are viewed as breeding grounds for arriving potentially new mechanisms in understanding ferromagnetism in materials. It has therefore become necessary to synthesize diluted magnetic semiconductors with phase purity. Despite significant advances in metal-doped nanocrystals, the crystallographic quality and purity of doped nanocrystals remain difficult to control. It is already established² that material properties depend strongly on precursors and synthesis methods in correlation with the thermodynamic process parameters. A number of reports^{2,3} are available on the synthesis of metal-doped anatase using high-temperature annealing, sol–gel technique, spray pyrolysis, and so on. The resulting sample consists of anatase as the dominant phase with small amounts of rutile and brookite phases of TiO₂. It means high-temperature methods can produce metal-doped anatase, which is in coexistence with unwanted rutile form in varying proportions. That is, assembling of metal-doped TiO₂ nanocrystals consisting of pure anatase crystal phase without significant phase transformation to rutile form is still a challenge. However, no reports on the photomediated^{8–11} synthesis of cobalt-doped nanosized titanium dioxide (nano-TiO₂) existing in anatase crystal form without any partial transformation to rutile phase have been published.

It is highly difficult to fabricate high-quality phase pure metal-doped anatase crystals because of anatase-to-rutile phase transformation. Second, despite a large number of theoretical predictions and experimental investigations, there is still no consensus on the origins of the ferromagnetic (FM) state in TiO₂/Co crystals. This investigation is aimed to obtain phase pure cobalt-doped anatase, followed by a systematic study on the structural and magnetic properties of TiO₂/x%Co nanocrystals (*x* in at %). Evolution of the surface structure was monitored using solid-state diffusion reflectance (UV–vis DRS), powder X-ray diffraction (PXRD), vibrating sample magnetometry (VSM), photoluminescence (PL), X-ray fluorescence (XRF), scanning electron microscopy (SEM), high-resolution transmission electron microscopy (HRTEM), X-ray photoelectron spectroscopy (XPS), and micro-Raman analytical techniques. Better knowledge of the effects of doping on nano-TiO₂ will aid in the invention of new ferromagnetic materials as well as the improvement of the present ones.

2. EXPERIMENTAL SECTION

A. Materials and Instrumentation Methods. Titanium tetraisopropoxide (99.99%), cobalt(II) chloride (99.9%), methyl amine (AR), and polyvinyl pyrrolidone (PVP-10) were obtained from Aldrich and used without purification. All other chemicals were of high grade quality and used as received. Photoreactions were carried out in a cylindrical quartz immersion well of 80 mL capacity (model 3210) using a low-pressure mercury vapor lamp, 254 nm, 6W as the light source for irradiation, (Germicidal G4T5, 3H, model 3006, Photochemical Reactors, Berkshire, U.K.). UV–vis diffuse reflectance spectra (UV–vis DRS) were recorded in absorbance mode at room temperature in the range 200–1000 nm on a Shimadzu, (UV 2450) double-beam spectrophotometer equipped with integrating sphere attachment (ISR-2200) using BaSO₄ as the reference. The instrument is interfaced with a computer for data collection and analysis. Fourier transform infrared (FTIR) spectra were recorded in the range 2000–400 cm^{−1} using a Thermo Nicolet 6700 FTIR spectrophotometer using KBr wafer with resolution 0.1 cm^{−1}. PXRDs were collected on an 800 W Philips (PANANALYTICAL, Almelo, The Netherlands) powder diffractometer equipped with an etched glass plate sample holder by rotating anode diffractometer in the 2θ range 10–80° with step size of 0.02° using Cu Kα (λ = 1.5406 Å) radiation to determine the identity of any phase and their crystalline size. Magnetization measurements were observed on a VSM, quantum design magnetic property measurement system (Lake Shore, 7404) equipped with a reciprocating sample option (vibration frequency: 82.5 Hz; magnet: 4'' (2'' at Pole face); max field: 15 kGauss; moment range: 1 μemu to 56 emu; and 80–1400 K temperature).

Room-temperature PL was recorded with a Horiba-Jobin Yvon, SPEX-SF13-11 spectrofluorimeter using 450 nm excitation wavelength from xenon lamp. XRF measurements were performed on wavelength-dispersive XRF spectrometer (Wd-Xrf) Bruker S4 PIONEER, with permanent output of 4 kW, standard collimators aperture angles of 0.15 and 0.46°, 0.077° collimator for high-resolution measurements and SPECTR Aplus software package for X-ray spectrometers (version 1.6). Surface morphology and chemical mapping were examined by SEM (Hitachi, S-3400N microscope), operating at 0.3–30 kV. Microanalyses (energy dispersive X-ray analysis, EDX) were performed with Thermo SuperDry II attachment of SEM. For TEM investigations, the samples were prepared by placing a drop of oxide powder and ultrasonically dispersing in alcohol. Microstructure analysis was undertaken on high-resolution transmission electron microscope (HRTEM) JEM 3010 JEOL (Tokyo, Japan) equipped with a field emission gun operating at 200 kV, a high brightness LaB₆ filament electron source, and image processing by digital micrograph software. X-ray photoelectron spectra were acquired on SAGE 100 spectrometer (SPECS) using a Mg Kα source operating at 20 mA and 12.5 kV. The experimentally observed binding energies of peaks were corrected for the binding energy of the Ti 2p_{3/2} peak located at 459.32 eV. Raman spectra were collected on the Jobin Yvon Horibra LABRAM-R1100 micro-Raman spectrophotometer with laser source He–Ne 633 nm and argon 488 nm.

*Synthesis of cis-[Co^{III}(en)₂(MeNH₂Cl)Cl₂]. cis-[Co^{III}(en)₂(MeNH₂Cl)Cl₂] was synthesized¹² by substituting chloride ligand with AnalaR methyl amine¹³ in *trans*-[Co^{III}(en)₂Cl₂]Cl. About 2 g of the cobalt(III) complex was suspended in 1 mL of water in a mortar. To this, a definite amount of AnalaR methyl*

amine was added in drops with constant grinding to obtain a paste. A rosy red color was observed, and the grinding was continued for 1 h to get a homogeneous solid mass. The paste was then allowed to stand overnight in a desiccator and then repeatedly washed with alcohol to remove residue remains in the product. The methyl-amine-substituted complex was recrystallized twice using acidified water, dried, and preserved in a desiccator.

Synthesis of Nano-TiO₂ through Sol–Gel Method. Polyvinyl pyrrolidone (2 mL of 2.5 wt % of PVP-10; average molecular weight = 10 000; Sigma-Aldrich) was suspended¹⁴ in a mixture of 2 mL of 0.2 M HCl and 86 mL of ethanol. Polyvinyl pyrrolidone can act as a stabilizing agent for the colloidal TiO₂ particles when dissolved in this solution. To this mixture, 0.5 mL of titanium tetra isopropoxide (Aldrich) in 9.5 mL of ethanol was added slowly and dropwise at 0 °C with vigorous stirring. The resulting solution was peptized by further stirring for 3–5 h to give a transparent TiO₂ sol (1.8×10^{-2} M TiO₂). The sol was then subjected to thermal heating at 600 °C for 5 h to obtain fine powder, which was grounded well in a mortar repeatedly and kept at 600 °C for 30 min. Ultrafine crystals of nano-TiO₂ were collected, characterized, and preserved for further studies.

B. Photoassisted Surface Reconstruction of Anatase Nano-TiO₂. The addition of *cis*-[Co^{III}(en)₂(MeNH₂)Cl]Cl₂ complex to the TiO₂ slurry resulted in surface-adsorbed¹⁵ complex ion after definite time of equilibration at room temperature. The adduct thus serves as a preassembled surface compound precursor for the photoassisted generation of dopant and subsequent implantation into anatase lattice. In a typical procedure, calculated quantity of nano-TiO₂ (3.13×10^{-2} M) was first dispersed in triply distilled water ultrasonicated for 10 min to obtain homogeneity. Subsequently, recrystallized solid sample of the complex *cis*-[Co^{III}(en)₂(MeNH₂)Cl]²⁺ (3.95×10^{-3} M) (mole ratio, Ti/Co 2:1, ionic strength NaNO₃ = 1 M) was slowly added, vigorously stirred for 2 min, and dosed with light of wavelength $\lambda = 254$ nm for a definite time interval at 300 K. The existence of multiple reaction pathways for the Co(III) → Co(II) reduction could not be discounted in this stage. That is, UV irradiation could influence both (i) interfacial electron transfer of nano-TiO₂ (electron/hole) with adsorbate–cobalt(III) complex to generate surface active site:Co(II) species and (ii) ligand to metal charge transfer reduction (LMCT) of cobalt(III) coordination structure producing Co^{II}_{aq} ion. Therefore, it was tempting to extract and investigate the photocatalyst, cobalt-implanted nano-TiO₂ in two stages for comparison (i) before irradiation, light dosage = 0 s, and (ii) after definite time of irradiation, light dosage = 120, 240, 480, and 720 s in dim red light; the ultrafine crystals were isolated, washed repeatedly, and centrifuged. Therefore, the nanoscale crystals obtained were subjected to spectral, macrostructural, microstructural, and surface morphological analyses using instrumental methods.

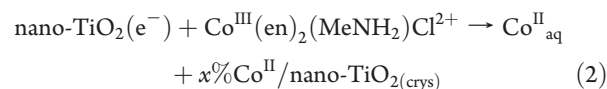
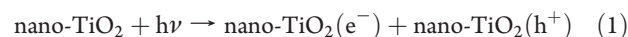
3. RESULTS AND DISCUSSION

A. Dopant Speciation and Substitution into Host Matrix.

A number of reports highlight the TiO₂ crystal phase transformation^{3,16} during doping, that is, when anatase is doped with transition-metal ion-like cobalt by annealing; a proportionate amount of anatase phase has become converted to rutile phase. It means high-temperature synthetic routes permit the appearance of impurity phase like rutile crystal phase during the formation of Co-doped anatase; moreover, the relative

concentration of rutile phase is the function of temperature and dopant concentration or both. Colloidal semiconductor has given, nowadays, a great impetus^{8,17,18} as a heterogeneous photocatalyst; the light absorption leads to the generation of electron–hole pairs in the particle that are oriented in a spatially random fashion along the path. The conduction band electrons and valence band holes undergo reaction with appropriate molecules in solution. The overall reaction is composed of (i) encounter complex formation of the electron/hole acceptor (molecular adsorbate) with semiconductor particles and (ii) interfacial electron transfer. Electron transfer between molecular adsorbates and bulk semiconductors involves electron transfer between discrete molecular states and a dense manifold of highly delocalized electronic levels in the solid. For nanomaterials that are not in the quantum-confined size regime, the electronic structure of the bulk material still applies, but there is a more significant contribution from surface defect states. Both delocalized band states and localized trap states may contribute to the electron transfer processes. Therefore, substrate-overlayer electronic interaction is obvious, and hence the promising photo-induced interfacial electron-transfer reaction could result. Co^{III}(en)₂(MeNH₂)Cl²⁺ ion addition into the dispersion of semiconductor particles led to the adsorption of complex ion on the semiconductor surface sites. Those surface sites generally accommodate^{18b} small molecules/ions. The defect sites on the TiO₂ surface influence prechemisorbed complex ion through electron transfer. The defect site consists of one oxygen vacancy and two Ti³⁺ ions (Ti³⁺–O[–]), which was found^{8,9,18} to act as an electron donor. Therefore, electron transfer from defect states occurs even in dark (at 0 s, before irradiation) but less efficiently. The integrity of nano-TiO₂ surface and thermodynamic considerations restricts formation of Co^{II} up to a minimum level of density, leading to the formation of 0.72%Co/nano-TiO₂ (at 0 s). An inner-sphere complex between *cis*-[Co^{III}(en)₂(MeNH₂)Cl]²⁺ with surface involves bond formation resulting in TiOH ↔ TiOCO^{II} → nano-TiO₂:Co^{II}_(crys) and subsequent generation of cobalt-implanted layer. The Co^{II} (ionic radius = 0.745 Å) diffuses³ into the lattice and preferably substitutes the Ti^{IV} (ionic radius = 0.68 Å) site; however, it depends upon the finite number of sites and site activity.

UV excitation of nano-TiO₂ injects an electron from the conduction band to the acceptor orbital of the cobalt(III) complex, producing Co(II) surface species. That is, interfacial electron transfer led to the reduction of the metal center Co(III) → Co(II), and the latter becomes surface active site:Co(II) species, which penetrates into the lattice to generate Co-doped TiO₂ lattice. The overall reaction taking place is nano-TiO₂ + $\lambda = 254$ nm + *cis*-[Co^{III}(en)₂(MeNH₂)Cl]Cl₂ → Co^{II}_{aq} + $x\%$ Co/nano-TiO₂ + products. The various process occurring are illustrated in eqs 1 and 2



The active site:Co(II) is anticipated to penetrate the anatase lattice, thereby reconstructing the surface layer of nano-TiO₂ (white) through octahedral substitution¹⁹ of Ti^{IV} sites, resulting in the formation of Co-doped nano-TiO₂ (gray) without any significant amount of phase transformation (rutile form). The amount of Co(II) implantation into the anatase lattice is a

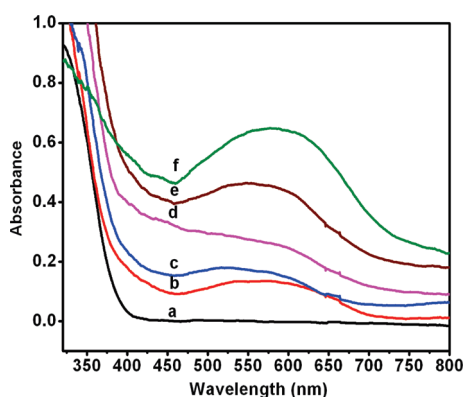
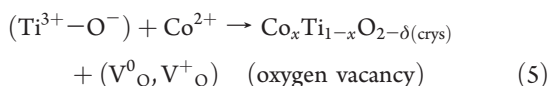
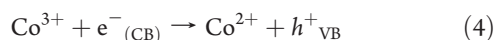
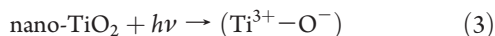


Figure 1. Diffuse reflectance spectra recorded for undoped and $x\%$ Co/nano-TiO₂ crystals with x ($\lambda = 254$ nm dosage time): (a) 0 (pure TiO₂), (b) 0.72 (0 s), (c) 0.91 (120 s), (d) 1.08 (240 s), (e) 1.14 (480 s), and (f) 1.26 at % (720 s) at 300 K.

function of light dosage. Ultimately, nonstoichiometric Co-doped semiconductor with varying dopant concentrations $x\%$ Co/nano-TiO₂ (where $x = 0.91, 1.08, 1.14$, and 1.24 at %) could be prepared through photoassisted implantation by increasing the dosage of light (changing time of irradiation: 120, 240, 480, and 720 s).

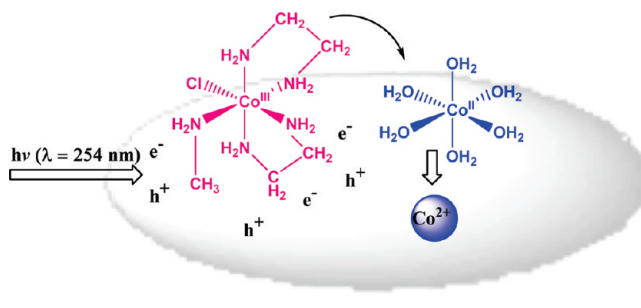
The mechanism of metal ion loading on the nano-TiO₂ lattice consists of injection of electron from the conduction band of TiO₂ to the d orbital of the preadsorbed species, leading to (i) the formation of Co-implanted nano-TiO₂ and simultaneously (ii) the creation of oxygen vacancy ($V^0_{\text{O}}, V^+_{\text{O}}$), as given in eqs 3–5.



This is consistent with the Co^{2+} ion substitutes for Ti^{4+} ions, with the balance of the charge compensated by $\text{O}_{2-\delta}$. A success in this step generally facilitates incorporation of Co^{II} into the nano-TiO₂ lattice occupying the cation sites (D_{2d} site symmetry) of anatase leading to Co-doped nano-TiO₂ crystals. Phase purity, crystallinity, surface modification, and microstructural investigations of the nanoparticles were carried out using spectral, magnetic, and electron microscopic analyses. This finding is rather surprising because in the literature phase pure doping is rarely achieved. Therefore, the focus here is on the characterization and analysis of the cobalt speciation in Co-doped nano-TiO₂ ($x\%$ Co/nano-TiO₂).

B. Identification of Cobalt(II) on the Surface of Anatase Nano-TiO₂. The optical properties of cobalt-implanted nano-TiO₂ were measured in a reflection mode. Absorption characteristics of nano-TiO₂ are greatly modified because of doping of the metal ions in the matrix. Figure 1 displays the diffuse reflectance spectra (DRS) of photoproducted $x\%$ Co/nano-TiO₂ crystals. DRS curves represent ultrafine crystals obtained at definite dosage periods, 120, 240, 480, and 720 s, compared with sample extracted before irradiation of light, that is, at 0 s. The DRS of undoped anatase showed 100% reflectance, and the doped samples absorb¹¹ more effectively in the range of 480–600 nm. A distinct absorption edge of $x\%$ Co/nano-TiO₂ is observed

Scheme 1. Formation of Surface Active Site:Co^{II} Species on Nanoparticle Anatase Surface through Photoinduced Interfacial Electron Transfer Reaction Employing UV Irradiation ($\lambda = 254$ nm)



in the 550–650 nm region with absorption maximum headed to a longer wavelength when at % of cobalt is increased. Semiconductor with low cobalt density $x = 0.72\%$ in $x\%$ Co/nano-TiO₂ absorbs at ~ 574 nm, and the λ_{max} shifts toward ~ 580 nm when x increases; that is, the extent of shifting depends upon the metal loading. The DRS reveals a red shift in the band gap transition, which can be explained by the introduction¹¹ of energy levels of the cobalt ion to the band gap of TiO₂. The shift to the red of absorption edge in $x\%$ Co/nano-TiO₂ has been attributed to the excitation of 3d Co^{2+} electrons into the conduction²⁰ band. At low concentration, ($x = 0.72$) Co^{II} ions can occupy regular Ti^{IV} sites substitutionally ($\text{Co}^{II}_{\text{Sub}}$), and at higher ion concentrations ($x = 1.26$ at %), they can also fill the interstitial sites ($\text{Co}^{II}_{\text{Int}}$). A more in-depth DRS analysis shows interesting results concerning absorption in the visible region that are useful in establishing the nature of the sites occupied by cobalt in the host lattice. The pattern indicates that Co^{II} entered into the lattice substitutionally, which is in favor of surface doping. The respective absorption edge is ascribed to arise because of contribution²⁰ of octahedral $\text{Co}^{II} \rightarrow \text{Ti}^{IV}$ intervalence charge transfer d–d transition. Moreover, the shift in absorption edge maximum is due to change in the band gap of titania, suggesting²¹ that a significant quantity of cobalt enters into a few surface sublayers of titania in octahedral coordination sites as Ti-substituted species, ($\text{Co}^{II}_{\text{Sub}}$), and a reasonable concentration could have entered interstitial positions, ($\text{Co}^{II}_{\text{Int}}$), because of the overlap of the 3d orbital of cobalt with semiconductor lattice. The DRS pattern is comparable to several diffuse reflectance spectra of Co-modified materials^{22,23} and Co/ZnO nanomaterial. In this connection, it is interesting to note a number of reports on the structure of $x\%$ Co/nano-TiO₂ prepared by annealing methods, which reveal that Co(II) enters into octahedral and interstitial tetrahedral sites. Scheme 1 illustrates the photogeneration of Co^{II} from surface-adsorbed $\text{cis}[\text{Co}^{III}(\text{en})_2(\text{MeNH}_2)\text{Cl}]^{2+}$ and subsequent implantation up to a few layers of surface of nano-TiO₂. The Co^{II} ions implanted on the surface occupy the D_{2d} distorted Ti^{IV} cation site of host anatase lattice, resulting in the formation of impurity donor states altering the Fermi level,^{16,19} as detailed in Scheme 2. The bands located at 550–650 nm are associated with n_2 absorptions due to the transitions: ${}^4\text{A}_2(\text{F}) \rightarrow {}^4\text{T}_1(\text{F})$ and ${}^4\text{A}_2(\text{F}) \rightarrow {}^4\text{T}_1(\text{P})$. These transitions often split into three components²⁴ because of the degeneracy lift of the excited levels ${}^4\text{T}_1(\text{P})$ and ${}^4\text{T}_1(\text{F})$ by spin–orbit coupling and the Jahn–Teller effect. Because Co^{II} is a weaker Lewis acid than Ti^{IV} , the cobalt

ions can be buried in the surface layers as interstitial species; some related studies confirmed the formation^{25,26} of tetrahedral species in Co-doping of anatase. Cobalt substitution in anatase would have facilitated the formation of defect structure.

FTIR spectroscopy has been used to investigate the vibrations of the TiO₂ crystal lattice, which are considerably affected by the presence of Co atoms. Furthermore, the anatase phase of *x*%,Co/nano-TiO₂ is in conformity with FTIR spectral data. Absorption

Scheme 2. Doping of Co^{II} into the Nano-TiO₂ Matrix Leading to the Formation of Impurity Donor Level of the Semiconductor, Where SC Is Surface Adsorbed Complex; Co^{III}(en)₂(MeNH₂)Cl²⁺

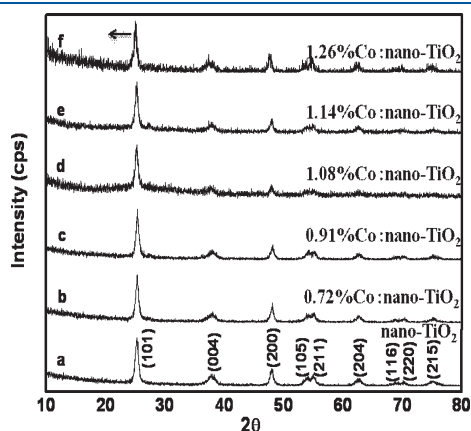
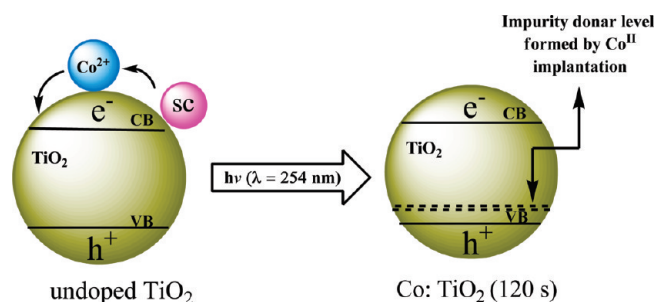


Figure 2. Powder X-ray diffraction pattern for undoped and *x*%,Co/nano-TiO₂ crystals with *x* ($\lambda = 254$ nm dosage time): (a) 0 (pure TiO₂), (b): 0.72 (0 s), (c): 0.91 (120 s), (d): 1.08 (240 s), (e): 1.14 (480 s), and (f) 1.26 at % (720 s) at 300 K.

peaks were observed between 450 and 600 cm⁻¹, which can be assigned to the Ti—O—Ti bond. Both the pure and Co-doped nano-TiO₂ showed a characteristic band at 507.4 cm⁻¹ corresponding to a Ti—O bond of the anatase phase²⁷ of nano-TiO₂. Moreover, the position of this Ti—O vibration tends to shift to lower energy as Co content in *x*%,Co/nano-TiO₂ is enhanced, indicating the existence of many more defects, especially oxygen vacancies. It is clear that some of the Ti^{IV} ions are substituted by the Co^{II} ions with simultaneous creation of oxygen vacancies.

C. Phase Pure Cobalt-Doped Anatase and Generation of Oxygen Vacancy. Primary structural information was given by XRD patterns of the photogenerated samples. Figure 2 depicts typical PXRD pattern of the pure and Co-doped samples, *x*%,Co/nano-TiO₂. The Co-doped nanosized crystals exhibit dominant peaks corresponding to the reflections of (101), (004), (200), (105), (211), (204), (116), (220), and (215) planes; these can be indexed to anatase tetragonal TiO₂ and are consistent with the standard reported^{27,28} values. Interestingly, the XRD patterns indicate phase pure anatase form and confirm the absence of appreciable phase transformation to other related crystalline phases like rutile and brookite. In addition, there are no X-ray reflections^{29,30} due to cobalt oxides or cobalt composites. However, an obvious shift of the (101) peak to a lower angle ($2\theta = 25.437$ to 25.051 , Figure 2a–f) is seen because of an increase²⁷ in the *d* value (Table 1) for the (101) lattice (3.5153 to 3.5565 Å; *x* = 0.72 to 1.26%) in Co-doped nanoparticles in comparison with the *d* value (3.4892 Å) of the (101) lattice in bare TiO₂ nanocrystals. An enhancement in *d* spacing implies a small elongation²⁸ of the unit cell along the *c* axis and *a* axis caused by substitution (Co^{II}_{Sub}) of smaller Ti⁴⁺ ion (0.745 Å) by larger Co²⁺ cation (0.792 Å). Figure 3 depicts the correlation between Co content versus *d*₁₀₁ and the average crystalline size calculated using the Scherrer relationship; both the *d*₁₀₁ value and the average crystalline size increase^{3,28} with respect to an enhancement in Co density in doped crystals. Recently, Li et al. showed³¹ the nonequilibrium solubility of dopant in rutile phase using X-ray pattern of *x*%,Co/nano-TiO₂. Therefore, the XRD patterns in Figure 2 correlate to a structured feature of anatase phase, which is indistinguishable even after intensive photolysis for a longer duration. Moreover, the diffraction peak becomes sharp as the concentration of cobalt is enhanced from *x* = 0.72 (at 0 s) to 1.26% (at 720 s); this suggests the gradual attainment of high order in crystalline phase. The average crystallite size of the anatase phase obtained from the dominant (101) peak is found to increase from 10.8 to 16.3 nm. A gradual increase in lattice constant *c* from 9.4217 to 9.4878 Å may be due to lattice

Table 1. Lattice Parameters Obtained from XRD Data, Average Crystalline Size and Photoefficiency of Co^{II}_{aq} Formed by the Excited Nano-TiO₂ (3.13×10^{-2} M) Reduction of Co^{III}(en)₂(MeNH₂)Cl²⁺ (3.95×10^{-3} M) in Water^a

dosage (s) ^b	<i>x</i> %,Co/nano-TiO	average crystalline size (nm)	photoefficiency of Co ^{II} _{aq} (%)	lattice parameter			
				<i>a</i> = <i>b</i> (Å)	<i>c</i> (Å)	volume Å ³	<i>d</i> ₁₀₁ (Å)
0	pure nano-TiO ₂	10.8	0.00	3.7567	9.4217	132.96	3.4891
0	0.72%,Co/nano-TiO ₂	11.0	0.00	3.7567	9.4298	133.25	3.5153
120	0.91%,Co/nano-TiO ₂	11.3	9.74	3.7567	9.4326	133.39	3.5157
240	1.08%,Co/nano-TiO ₂	11.7	13.77	3.7808	9.4574	133.85	3.5235
480	1.14%,Co/nano-TiO ₂	13.6	24.20	3.7808	9.4677	135.66	3.5263
720	1.26%,Co/nano-TiO ₂	16.3	34.34	3.7474	9.4878	138.23	3.5565

^a Wavelength of excitation, $\lambda = 254$ nm; ionic strength: 1 M NaNO₃; light intensity: 1×10^{18} Einstein s⁻¹. ^b Dosage of light in terms of time of irradiation of nanomaterial semiconductor particles.

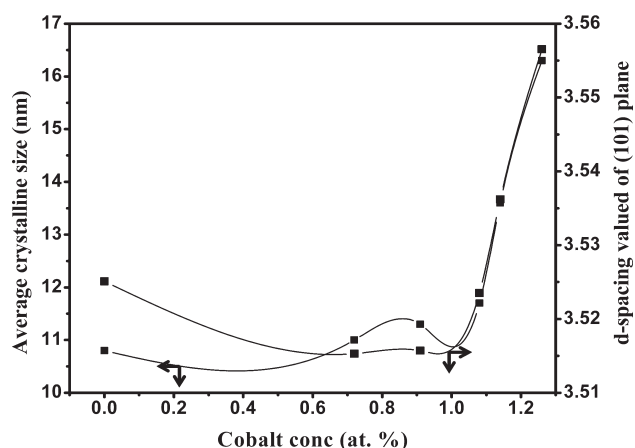


Figure 3. Plot of dopant concentration obtained from (SEM-EDX) for $\text{Co}_x\text{Ti}_{1-x}\text{O}_{2-\delta}$ versus average crystallite size and d -spacing value of (101) plane obtained from PXRD of pure and $x\%$ Co/nano- TiO_2 . Wavelength of irradiation ($\lambda = 254$ nm) $\text{Co}(\text{en})_2(\text{MeNH}_2)\text{Cl}^{2+}$ (3.95×10^{-3} M); nano- TiO_2 (3.13×10^{-2} M) at 300 K.

elongation in the z axis^{13,27} (Figure 2f), indicating considerable distortion in octahedral coordination sphere. Table 1 and Figure 3 imply that UV irradiation of nano- TiO_2 /adsorbate- $\text{cis}[\text{Co}^{\text{III}}(\text{en})_2(\text{MeNH}_2)\text{Cl}]\text{Cl}_2$ generate surface active site: $\text{Co}(\text{II})$, which readily migrates to the surface of nanocrystals substitutionally. Ultimately, substitution³² of Co^{II} for Ti^{IV} ion in the lattice balances the charge by $\text{O}_{2-\delta}$, which strongly argues the creation of oxygen vacancy ($\text{V}_{\text{O}}^{\bullet}$, V_{O}^{+}). Donor-type defects such as oxygen vacancies have been proposed to be key elements necessary for ferromagnetism in transition-metal-doped TiO_2 .

D. Ferromagnetism due to the Influence of Oxygen Vacancy. Magnetization versus field (M - H) curves for $x\%$ Co/nano- TiO_2 ($x = 0.72$ – 1.26 at %) crystals observed at room temperature are shown in Figure 4. A well-defined hysteresis loop with relatively high external field ~ 4000 Oe to achieve the saturation level is seen for the magnetization curve. The hysteresis loop represents distinct evidence, although response is weak, of the ferromagnetic ordering at room temperature (300 K). The magnetic susceptibility values, $\chi = -5.71 \times 10^{-6}$ to 1.19×10^{-5} , suggest the presence of the magnetic phase. The saturation moment (M_s) of the samples was estimated from the linear extrapolation of high field data. The saturation magnetic moment, μ_B , was calculated after the paramagnetic and diamagnetic contributions were corrected. The magnetization data collected for the Co/ TiO_2 samples show a very weak but temperature-independent value between 77 and 300 K that is consistent with the observation made by Gamelin et al.¹ for triethylphosphine oxide-capped $1.3\%\text{Co}^{2+}/\text{TiO}_2$ nanocrystals obtained by annealing method. The coercive field (H_c) is somewhat high (68.84 to 92.24 Oe) with appreciable remanence (M_R) values (0.02 to $1.44 \times 10^{-7} \mu_B/\text{Co}^{\text{II}}$) for $x = 0.91, 1.08, 1.14$, and 1.26 crystals at 300 K (Table 2). The 300 K ferromagnetic saturation moment is seen to reduce³³ appreciably with the Co density, $M_s = 14.40 \times 10^{-3} \mu_B/\text{Co}^{\text{II}}$ ($x = 0.72$ at %) and $M_s = 0.196 \times 10^{-3} \mu_B/\text{Co}^{\text{II}}$ ($x = 1.26$ at %) in which Co^{II} is in high spin configuration (spin = $3/2$). Field-dependent magnetization (M - H) measurements of photogenerated $x\%$ Co/nano- TiO_2 crystals exhibit ferromagnetism at room temperature. The narrow range of values indicates a common origin for the ferromagnetism and the magnetic hardness (H_c) and the magnetic parameters imply the increasing disorder in the Co-doped lattice.

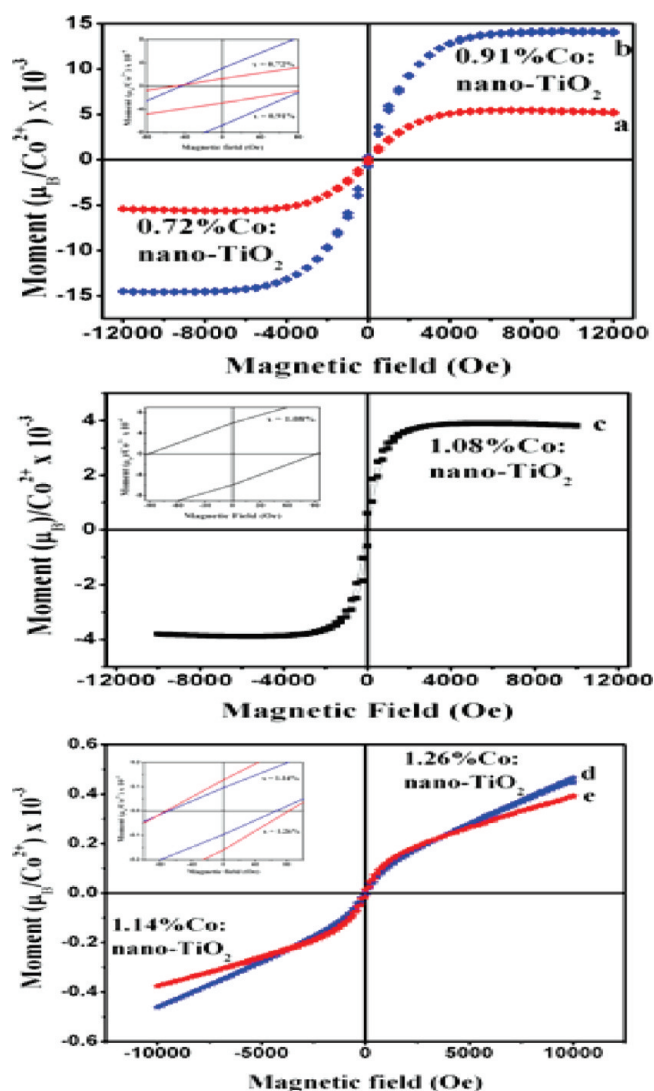


Figure 4. Room-temperature M - H hysteresis loops recorded for $x\%$ Co/nano- TiO_2 , where $x =$ (a) 0.72, (b) 0.91, (c) 1.08, (d) 1.14, and (e) 1.26 at % of Co at 300 K. The inset shows the coercivities of the powder samples. Note the different axis scale. All data have been corrected for diamagnetism.

Manivannan et al.^{3,28,47} reported that paramagnetic $\text{Co}_{0.1}\text{Ti}_{0.9}\text{O}_{2-\delta}$ prepared by sol-gel technique at 673 K upon hydrogenation acquired room-temperature ferromagnetism (RTFM). The ferromagnetism was found to be due to oxygen holes produced by H_2 , which extracted oxygen from the sample. Beyond this central observation, M values become weak when x increases in Co-doped anatase matrix of this work, which can be due to structure defects, substrate, lattice strain defects,² and deficiency^{11,25} of oxygen vacancies. The observed ferromagnetic ordering in photogenerated $\text{Co}_x\text{Ti}_{1-x}\text{O}_{2-\delta}$ samples can be justified by the creation of some sort of defect site in the sample. Li et al. showed³¹ weak ferromagnetism in metal-doped semiconductor, and the observation was explained due to the absence of metallic cluster or CoO . Ogale et al.³² investigated a mixed-state scenario for ferromagnetism for Co/TiO_2 film at 400 °C. Park et al. predicted²⁶ a rise in the spin magnetic moment of cobalt from 1 to $2.5 \mu_B$ using LMTO calculations, which was established to be due to an oxygen vacancy in the vicinity of a

Table 2. Magnetic Characteristics and EDX Data of Undoped and $x\%$,Co/nano-TiO₂ Crystals, Obtained from the Excited Nano-TiO₂ (3.13×10^{-2} M) Reduction of Co^{III}(en)₂(MeNH₂)Cl²⁺ (3.95×10^{-3} M) in Water at 300 K^{a,b}

dosage (s) ^c	$x\%$,Co/nano-TiO ₂	$\mu_B/\text{Co}^{\text{II}}$ (10^{-3})	magnetic susceptibility (χ)	coercivity (Oe)	remanence $\mu_B/\text{Co}^{\text{II}}$	EDX profile (at %)		
						Ti	O	Co
0	nano-TiO ₂	0	0	0	0	33.33	66.67	0.00
0	0.72%,Co/nano-TiO ₂	14.40	-5.71×10^{-6}	69.31	00.020	32.88	66.40	0.72
120	0.91%,Co/nano-TiO ₂	5.580	-5.13×10^{-6}	81.07	00.014	32.73	66.36	0.91
240	1.08%,Co/nano-TiO ₂	3.950	-1.06×10^{-4}	92.24	8.87×10^{-6}	32.61	66.31	1.08
480	1.14%,Co/nano-TiO ₂	0.301	$+9.07 \times 10^{-6}$	68.84	1.44×10^{-7}	32.58	66.29	1.14
720	1.26%,Co/nano-TiO ₂	0.196	$+1.19 \times 10^{-5}$	77.96	2.28×10^{-7}	32.49	66.25	1.26

^a Wavelength of irradiation, $\lambda = 254$ nm. Ionic strength: 1 M NaNO₃. Light intensity: 1×10^{18} Einstein s⁻¹. ^b Relative permeability (μ_r) 0 for nano-TiO₂, 1.0 N A^{-2} for $x\%$,Co/nano-TiO₂ ($x = 0.72, 0.91, 1.08, 1.14$, and 1.26 at %). ^c Dosage of light measured in terms of time of irradiation.

substitutional cobalt ion that enhanced the value. Janisch et al.³³ and Coey et al.³⁴ in separate studies concluded that Co^{II} ions substituted for Ti^{IV} cations in anatase TiO₂ matrix led to a lowest energy magnetic configuration, which is the ferromagnetic one. Indeed, more prominent hysteresis loops were observed for the photogenerated Co_xTi_{1-x}O_{2-δ} crystals in this investigation. Therefore, ferromagnetism of the cobalt-doped nanocrystals indicates the substitutional behavior of dopant ion rather than formation of precipitates of metal/metallic oxides. Accordingly, the ferromagnetism is addressed by the presence of oxygen vacancies. This is similar to observations in Co-doped titanium dioxide films, nanotubes, and nanoparticles, where the presences of oxygen vacancies along with Co²⁺ ions were found to be essential for the observation of RT ferromagnetic ordering. Sullivan et al.³⁵ proved that cobalt ion enters interstitially in anatase matrix under oxygen poor conditions, but penetration at the secondary grain boundaries³¹ is much less probable. Chambers and coworkers³⁴ reported that the ferromagnetism of $x\%$,Co/nano-TiO₂ strongly depends on the number of oxygen vacancies in the lattice when Co^{II} substitutes Ti^{IV} in the lattice. Because of high dielectric permittivity of TiO₂ (the refractive index is ~ 2.49), a large-radius trapping center is formed at the oxygen vacancy site. This extended electron state effectively couples neighboring cobalt ions, forming a homogeneous ferromagnetic state in the diluted $x\%$,Co/nano-TiO₂ system. Hence, more extended electron orbital at trapping center could provide a large value of exchange interaction that couples^{25,33–36} to the local spin of cobalt ion becoming ferromagnetic.

Because the tetravalent Ti^{IV} ion is substituted by divalent Co^{II}, there are intrinsic oxygen vacancies (V⁰_O, V⁺_O) in the doped system to compensate charge discrepancy, and the substitution has the effect of adding two holes to the system and half-filled oxygen vacancy states (F-centers). The observation of decrease in M_s with respect to increase in Co concentration $M_s = 14.4 \text{ m}\mu_B/\text{Co}^{\text{II}}$ ($x = 0.72\%$) to $0.196 \text{ m}\mu_B/\text{Co}^{\text{II}}$ ($x = 1.26\%$) is due to the fact that oxygen vacancy³⁷ prefers to stay near cobalt and majority of (V⁰_O, V⁺_O) are bound to Co^{II}_{sub} to become (Co^{II}_{sub}/V⁰_O, V⁺_O) complex. The appearance of ferromagnetism in the Co-doped TiO₂ lattice also strongly depends on the formation and distribution of donor-type defects such as oxygen vacancies and their tendency to form^{34b} complexes with Co atoms. It causes the magnetic moment to further decrease because of the lack of oxygen vacancy in conjunction with the effect of interstitial cobalt destroying^{37–40} the spin polarization of the substitutional cobalt nearby.

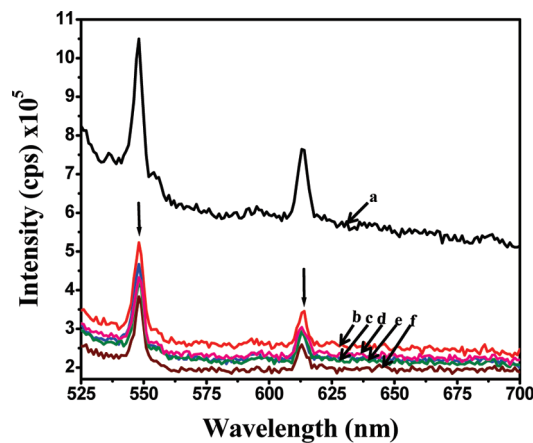


Figure 5. Photoluminescence spectra for undoped and Co_xTi_{1-x}O_{2-δ} crystals with x ($\lambda = 254$ nm dosage time): (a) 0 (pure TiO₂), (b) 0.72 (0 s), (c) 0.91 (120 s), (d) 1.08 (240 s), (e) 1.14 (480 s), and (f) 1.26 at % (720 s) at 300 K.

Photoluminescence (PL) is an effective tool to study the lattice defects in the diluted magnetic semiconductor samples. As shown in Figure 5, strong green emission at 548 nm and moderate emission at 613 nm are observed because of excitation using 450 nm (xenon source). The emission characteristics of Co_xTi_{1-x}O_{2-δ} ($x = 0.72$ to 1.26 at %) are quite similar to that of undoped nano-TiO₂, however, emission intensity drastically reduced for the former cases. Very recently, Majima et al. have reported³⁹ strong green emission of ZnO nanocrystals at 510–530 nm. Therefore, emissions likely originate from (i) surface defects, such as ionizable oxygen vacancies (V⁰_O, V⁺_O, etc.) or titanium vacancies (V⁻_{Ti}, V²⁻_{Ti}, etc.). In the basic TiO₂ cell, each Ti^{IV} is surrounded by an octahedron of six O²⁻ ions; structural defect can be formed by the loss of a neutral oxygen atom during photoinduced incorporation of cobalt⁴⁰ into host matrix. However, the defect states associated with Ti^{III} ions are introduced in the band gap at 0.7 to 0.8 eV below the energy of Fermi level.⁴¹ The PL emission may also be possible because of (ii) the recombination of self-trapped excitons (STEs) localized⁴² within TiO₆ octahedra. The STE in the present samples originate from band-to-band excitation where the excited electron and the hole create a local deformation of TiO₆ octahedra and thus localize themselves into surface defect states of TiO₂. Moreover, the 548 nm emission of Co_xTi_{1-x}O_{2-δ} can be regarded as a combination of two emissive states such as: (i) STEs and (ii) oxygen vacancies. In a recent report, the shallow

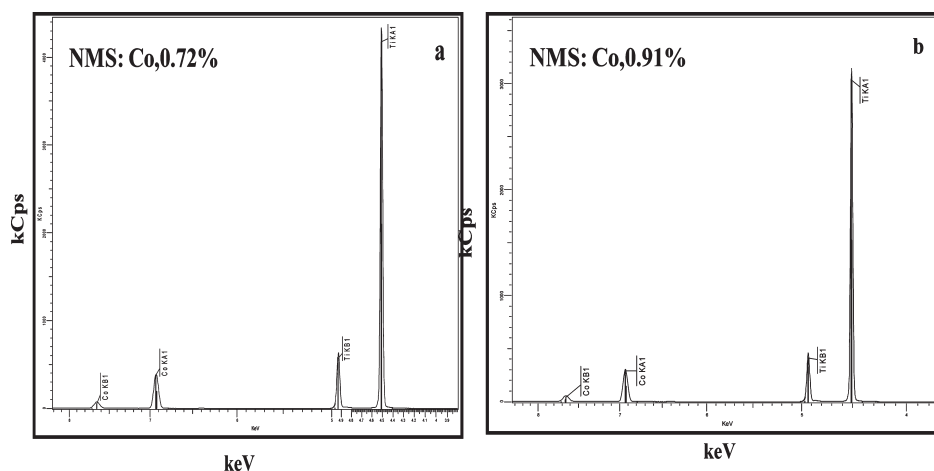


Figure 6. X-ray fluorescence spectra for $\text{Co}_x\text{Ti}_{1-x}\text{O}_{2-\delta}$, where $x =$ (a) 0.72 (0 s) and (b) 0.91 (120 s) at % at 300 K.

Table 3. Chemical Contents in $\text{Co}_x\text{Ti}_{1-x}\text{O}_{2-\delta}$ Crystals Using X-ray Fluorescence Analysis, Cobalt-Doped Nano- TiO_2 Generated by the Photomediated Implantation of Co(II) into the Anatase Lattice^a

element	density of Co, x in $\text{Co}_x\text{Ti}_{1-x}\text{O}_{2-\delta}$				
	0.72	0.91	1.08	1.14	1.26
Ti	93.76	93.2	93.2	93.0	92.8
Co	4.93	5.34	5.39	5.51	5.93
Cl	0.12	0.13	0.13	0.15	0.11
Na	0.53	0.55	0.62	0.61	0.55
S	0.10	0.12	0.11	0.13	0.09
Si	0.17	0.25	0.26	0.27	0.27
total	99.61	99.59	99.71	99.67	99.75

^a $\text{Co}^{\text{III}}(\text{en})_2(\text{MeNH}_2)\text{Cl}^{2+}$ (3.95×10^{-3} M); nano- TiO_2 (3.13×10^{-2} M) in water at 300 K. Ionic strength: 1 M NaNO_3 . Wavelength of excitation, $\lambda = 254$ nm; light intensity: 1×10^{18} Einstein s^{-1} .

traps were identified³⁹ because of oxygen vacancies lying⁴³ at 0.51 eV below the conduction band of TiO_2 matrix. In this investigation, a gradual decrease in PL intensity at 548 and 613 nm emissions was observed for $\text{Co}_x\text{Ti}_{1-x}\text{O}_{2-\delta}$ crystals when x was increased from 0.72 to 1.26%. A plausible explanation for this result is that the dopant induces geometrical distortions (contractions) of the neighboring oxygen vacancy,³⁷ and hence the emission intensity is altered.

XRF analysis is a commonly recognized⁴⁴ efficient method for the qualitative and quantitative determination of the material composition by sample irradiation with high-energy photons (X- or γ -rays). Figure 6 presents the XRF of the nanomaterial crystals 0.72%,Co/nano- TiO_2 and 0.91%,Co/nano- TiO_2 . Two prominent peaks are observed representing titanium and cobalt; the one with the high intensity peak is due to primary X-rays, and the other one is due to secondary X-rays. The presence of high intensity peaks for titanium is observed at 4.5 ($k\alpha$) and 4.9 keV ($k\beta$), and the peaks at 6.9 ($k\alpha$) and 7.65 keV ($k\beta$) are attributed^{1,2} to cobalt ion. The absence of any other peak obviously indicates that the nanomaterials under study are free from impurities. The intensity (Table 3) of prominent Co peak is found to increase from 4.93 (kCps) ($x = 0.72$) to 5.34 (kCps) ($x = 0.91$ Co at %); it appears that the rise in dopant density aids to produce defect states in nano- TiO_2 lattice. XRF measurements

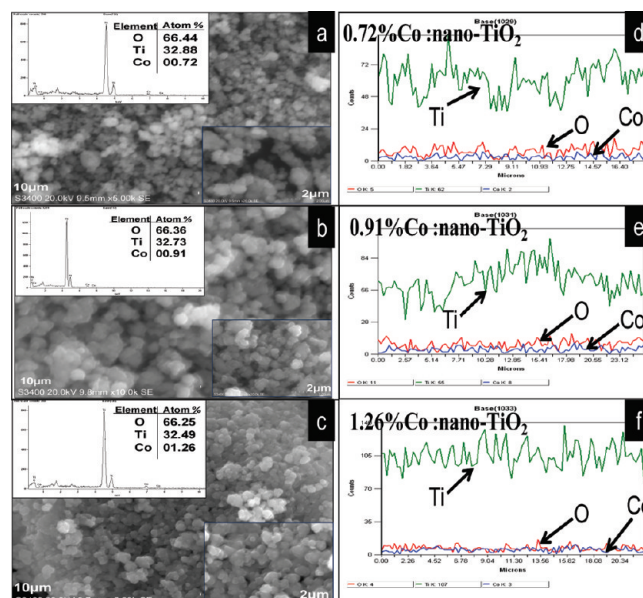


Figure 7. SEM images, EDX, and line scan spectra for $x\%$ Co/nano- TiO_2 , where $x =$ (a,d) 0.72, (b,e) 0.91, and (c,f) 1.26 at % of Co at 300 K.

dictate that there are primarily titanium and cobalt cations, in agreement with a state of high chemical purity of $\text{Co}_x\text{Ti}_{1-x}\text{O}_{2-\delta}$ samples.

E. Surface Morphology and Crystalline Phase. SEM analysis was employed to understand and monitor the surface morphology and surface composition of $\text{Co}_x\text{Ti}_{1-x}\text{O}_{2-\delta}$ crystals. Figure 7 depicts SEM images, which illustrate that the particles mainly belong to anatase phase, loosely agglomerated, spherical with a few hundred nm in size, and significantly good in crystalline quality. Figure 7a–f consists of high- and low-resolution images along with line spectrum and EDX profile for $\text{Co}_x\text{Ti}_{1-x}\text{O}_{2-\delta}$, ($x = 0.72, 0.91$, and 1.26 Co%) crystals. They exhibit a nearly uniform blend of spherical morphology and the crystals composed of grains of similar size with randomly distributed pores. Homogeneous and continuous surface structure with well-dispersed spheres appears as the dopant density in $\text{Co}_x\text{Ti}_{1-x}\text{O}_{2-\delta}$ is increased; moreover, a gradual improvement in crystallinity is remarkably observed. The inset EDX (Figure 7a–c) is the micro-analysis data used to determine the elementary composition and

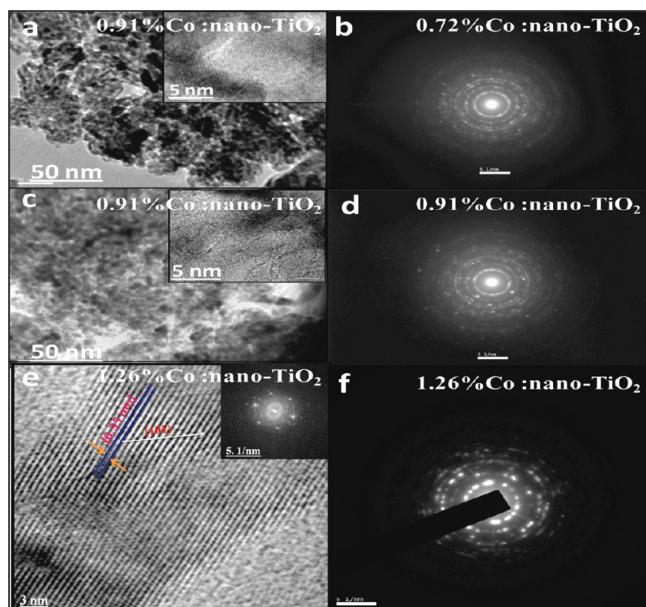


Figure 8. Transmission electron microscopic images, lattice fringes, and SAED for $x\%$ Co/nano-TiO₂, where $x =$ (a,b) 0.72, (c,d) 0.91, and (e,f) 1.26 at % of Co at 300 K.

mainly to confirm the presence of cobalt dopant⁴⁵ within the titania lattice. EDX data reveal (Table 2) that the concentration of cobalt dopant is linearly dependent on the dosage of light during the synthesis of Co_xTi_{1-x}O_{2-δ}. The occurrence of elemental (cobalt) distribution in EDX is well-dispersed throughout the granule, and the line spectra (Figure 7d–f) show a good chemical homogeneity ($x = 0.72, 0.91$, and 1.26 at %) of samples. However, a significant amount of exchange between the counts of Co and O is noted in the whole range of the line spectrum. Such exchange of counts is beyond the statistical fluctuation of the data due to uneven surface. This information is relevant to presume the presence of antisite disorder (exchange interaction of Co and O sub lattices) prior to Ti substitution. The line spectra of Ti, O, and Co (Figure 7e–f; $x = 0.91$ and 1.26) are relatively uniform in comparison with the spectrum of Ti, O, and Co (Figure 7a; $x = 0.72$). Thus, the large exchange interaction between Co and O in the samples accounts for structural disorder⁴⁶ in nano-TiO₂ lattice.

High-resolution transmission electron microscopy was used to determine the morphology and the crystalline phases of the undoped and Co-doped nano-TiO₂. The Co_xTi_{1-x}O_{2-δ} crystals are mostly spherical with diameter in the range of 4–14 nm with an average value of 5–10 nm. The surface of the particles consists of large, light column regions with columns growing out of the surface roughly circular and has dimensions of approximately 15–20 nm. Figure 8a–f provides both low- and high-resolution images of the nanosized Co_xTi_{1-x}O_{2-δ} crystals ($x = 0.72, 0.91$, and 1.26 at %). The high magnification and SAED patterns, show uniform lattice planes of TiO₂ and spotty ring pattern (consist of Debye–Scherrer rings); each ring corresponds to particular hkl reflection of the identical phase. The dark-field image was taken by measuring the strongest ring (101) plane of TiO₂. The selected area electron diffraction (SAED) patterns confirm that the Co-doped anatase shows good crystallinity with loosely agglomerated spherical particles. Dispersion of particles, formation of pseudohexagonal pattern, and the quality of crystallinity

are highly gradual^{8,10} when the dopant content is increased from $x = 0.72$ to 1.26 Co%. SAED studies exhibit purity and crystallinity (Figure 8b,d,f), in which the spotty ring patterns reveal the existence of phase purity of anatase host matrix. Moreover, SAED shows the absence of any impurity in anatase crystalline phase such as cobalt oxides or metallic cobalt. The first four main sharp diffraction rings illustrate the (101), (004), (200), and (211) reflections^{28,46} in Co_xTi_{1-x}O_{2-δ} samples. The lattice fringes attribute to an interplanar distance of ~ 0.35 nm, which is characteristic of the (101) plane of anatase TiO₂ lattice. The inset (Figure 8e) shows the fast Fourier transform (FFT) patterns of the 1.26% Co/nano-TiO₂, which supports the (101) plane of the anatase TiO₂. Figure 8f ($x = 1.26$ at %) displays well-resolved lattice fringes pointing to the higher-order crystallinity and assignable to hkl reflection. HRTEM results closely resemble those of XRD observations.

XPS experiments were carried out to sense the chemical status of cobalt ion in Co_xTi_{1-x}O_{2-δ}, and Figure 9 depicts the XPS spectra of nano-TiO₂ along with $x = 0.72$ and 0.91 at % crystals. Table 4 lists the experimental binding energies measured for the Co-doped crystals and reported values of Co 2p peaks for cobalt metal and cobalt oxides. The core-level Ti 2p were observed at ~ 464 (Ti 2p_{1/2}) and at ~ 459 eV (Ti 2p_{3/2}) after carbon correction, which can be assigned^{46–50} to the Ti^{IV} in anatase TiO₂. The characteristic⁴³ shift in the cation (Ti 2p) core-level position implies the incorporation of cobalt into the Ti site of anatase lattice and subsequent formation of oxygen vacancy. Furthermore, the difference in binding energies (ΔE) between O 1s_{3/2} and O 1s_{1/2} peaks (Table 4) is more pronounced in crystals with $x = 0.72$ and 0.91 than in pure anatase matrix; such observation is rationalized by the argument that the formation of oxygen vacancy defects is associated with electronic charge transfer⁴⁷ from the anion (oxygen) to cation (titanium). Figure 9 shows the Co 2p core level spectrum of Co/TiO₂ ($x = 0.72$ and 0.91); the Co 2p_{1/2} and Co 2p_{3/2} peaks arise at ~ 798 and 781.7 eV respectively, with a peak separation (ΔE) of 16.3 eV and two shake-up peaks at ~ 804 (Co 2p_{1/2}) and 787 eV (Co 2p_{3/2}). The shake-up peaks are identified to be characteristic of the chemical state of cobalt in the lattice and indicate⁵¹ the presence of Co^{II}. Strong paramagnetic satellite peaks are consistent^{3,22} with the presence of CoO, Co₂O₃, or mixed-valent Co₃O₄ and are not detected in this study. This is an indication of absence of Co⁰ and oxides of cobalt in Co_xTi_{1-x}O_{2-δ} crystals. On the basis of all of this collective evidence, it is confirmed that Co/TiO₂ is a DMS system and creation and distribution of oxygen vacancies in the Co_xTi_{1-x}O_{2-δ} lattice^{47–51} dictate ferromagnetism.

Raman spectra were used to identify the crystalline phase of Co_xTi_{1-x}O_{2-δ} matrix; according to symmetric properties, six Raman active modes are predicted^{52,53} for anatase phase. The characteristic modes are E_g : 147 cm^{-1} ; E_g : 198 cm^{-1} ; B_{1g} : 398 cm^{-1} ; A_{1g} and B_{1g} : 515 cm^{-1} ; and E_g : 640 cm^{-1} . The rutile phase consists of predominant modes appearing at E_g : 448 cm^{-1} ; A_{1g} : 448 cm^{-1} ; and B_{1g} : 827 cm^{-1} . Figure 10 clearly indicates the Raman frequencies characteristic of anatase phase and the absence⁵⁴ of rutile phase. Moreover, Raman vibrational modes representing secondary phases like metallic cobalt, cobalt oxides, and Co–Ti oxide species are absent, eliminating the possible formation of segregated cobalt oxide in Co_xTi_{1-x}O_{2-δ} crystals. The B_{1g} (398 cm^{-1}) peak is a good calibrant of anatase phase for the undoped and doped crystals. Within the experimental accuracy of a few wave numbers, there is a discernible shift and broadening of the B_{1g} at 398 and E_g at 640 cm^{-1} peaks with

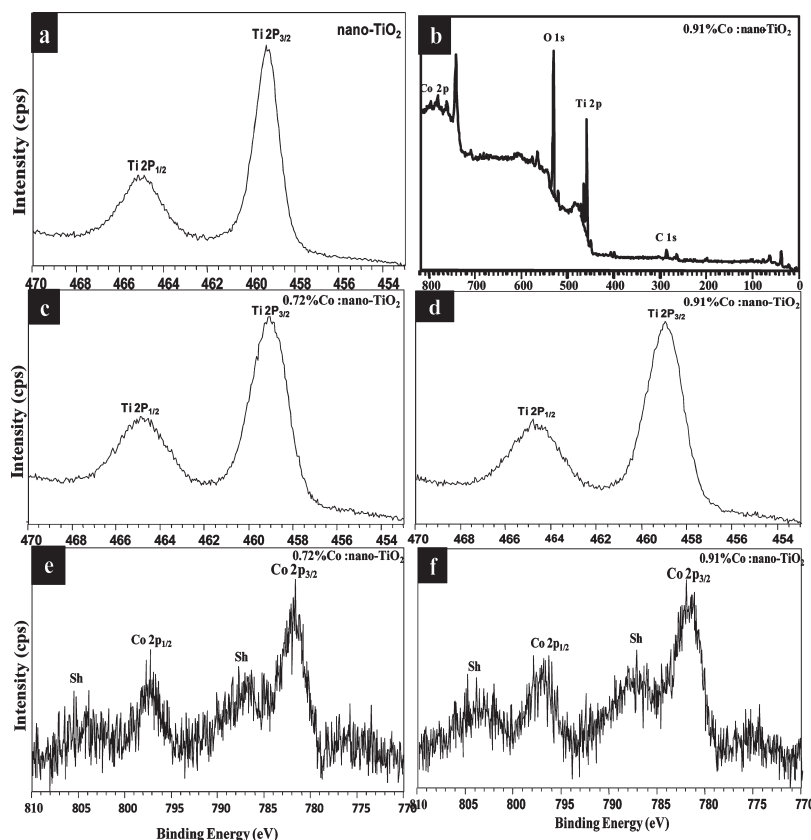


Figure 9. XPS spectra for undoped and $\text{Co}_x\text{Ti}_{1-x}\text{O}_{2-\delta}$, where $x = (\text{a,c,e})$ 0.72 and (d,f) 0.91 at % of Co at 300 K.

Table 4. X-ray Photoelectron Spectroscopic Data for Pure Nano-TiO₂, $\text{Co}_x\text{Ti}_{1-x}\text{O}_{2-\delta}$, Cobalt, and Oxides of Cobalt^{a,b}

dopant density x	dosage (s)	binding energy (eV)									
		titanium 2p (eV)			oxygen 2p (eV)			cobalt 2p (eV)			B.E (eV) ^{3,47–50}
		Ti 2p _{1/2}	Ti 2p _{3/2}	ΔE	O 1s _{1/2}	O 1s _{3/2}	ΔE	Co 2p _{1/2}	Co 2p _{3/2}	ΔE	
nano-TiO ₂	0	464.98	459.32	5.66	530.48	531.78	1.30				
0.72%	0	464.74	459.10	5.64	530.25	532.28	2.03	798	781.66	16.34	780.82
0.91%	120	464.66	459.04	5.62	530.22	532.49	2.27	798	781.72	16.28	780.82
Co											778.30
Co ₃ O ₄											779.30
Co ₂ O ₃											779.90
CoO											780.00
CoO multiplet splitting											786.30
Co ^{III} ion											779.9

^a Cobalt-doped nano-TiO₂ generated by the photomediated implantation of Co(II) into the anatase lattice. $\text{Co}^{\text{III}}(\text{en})_2(\text{MeNH}_2)\text{Cl}^{2+}$ (3.95×10^{-3} M); nano-TiO₂ (3.13×10^{-2} M) in water at 300 K. Wavelength of excitation, $\lambda = 254$ nm; light intensity: 1×10^{18} Einstein s^{−1}. Ionic strength: 1 M NaNO₃.

^b Shake-up peaks observed for Co 2p/Co 2p_{1/2} and Co 2p_{3/2} = 804 and 787.2, $\Delta E = 16.8$ ($x = 0.72$ at %); Co 2p_{1/2} and Co 2p_{3/2} = 804 and 786.9, $\Delta E = 17.4$ ($x = 0.91$ at %).

higher doping concentration, which implies limited Co solubility and changes in surface structure. That is, broader Raman peaks between 400 and 700 cm^{−1} represent⁵² strong cobalt–surface interaction and nonstoichiometric character of the surface layer but different from spinel structure. Obviously, it can be concluded that photomediated implantation of Co on the surface of nano-TiO₂ does not alter the crystal phase and simultaneously generates oxygen vacancies.⁵⁵ Such inference is parallel^{3,56} to a Raman study on Co-doped TiO₂ nanotubes and nanoparticles.

In addition, the prominent peak signal E_g at 147 cm^{−1} intensity decreases drastically in tune with considerable shifts of less intense and broader peaks due to inclusion^{57,58} of Co^{II} in $x\%$, Co/nano-TiO₂ matrix. It means the vibrations of TiO₂ crystal lattice are considerably affected by the inclusion of Co^{II} atoms^{3,28} and confirms dopant implantation. It has also been reported that the shift and broadening of Raman peaks^{59,60} are caused due to the nonstoichiometric character of nano-TiO₂ by the existence of oxygen vacancies.

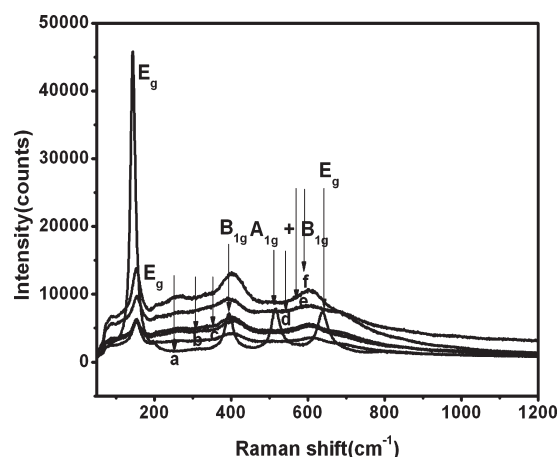


Figure 10. Micro Raman spectra for undoped and $\text{Co}_x\text{Ti}_{1-x}\text{O}_{2-\delta}$, where $x =$ (a) 0, (b) 0.72, (c) 0.91, (d) 1.08, (e) 1.14, and (f) 1.26 at % of Co at 300 K.

4. CONCLUSIONS

This investigation focuses on the successful synthesis of high-quality nanoscale crystals, $x\%$, Co/nano- TiO_2 of single-phase anatase structure by UV-induced Co^{II} implantation into the host matrix. The method makes use of incorporation of photoproduced Co^{II} dopant from surface-adsorbed cobalt(III) complex ion to tailor the crystalline phase. Higher light dosage enhances the incorporation of Co density into the matrix dramatically. Optical measurements have revealed that the incorporation of cobalt(II) ions into the titania crystal lattice, which ultimately decreases the band gap energy value. XRD analysis confirmed that penetration of dopant ions has not effected partial transformation of anatase phase to undesirable rutile impurity phase. Magnetization measurements of $\text{Co}_x\text{Ti}_{1-x}\text{O}_{2-\delta}$ as a function of applied field and temperature showed significant magnetic moment of $(14.40 \text{ to } 0.196) \times 10^{-3} \mu_{\text{B}}/\text{Co}^{\text{II}}$ with hysteresis loops in the range $-4000 < H < +4000$ Oe at 300 K at room temperature. This experimental result indicates that impurity clustering is not essential to obtain ferromagnetism in diluted magnetic semiconductors, but oxygen vacancy, $(\text{V}_{\text{O}}^{\bullet}, \text{V}_{\text{O}}^+)$ contributes significantly. The direct evidence of the compositional inhomogeneity of $\text{Co}_x\text{Ti}_{1-x}\text{O}_{2-\delta}$ compound was given. XPS results show that Co is primarily in the +2 oxidation state. Cobalt-doped nano- TiO_2 was characterized by PL, XPS, electron microscopic, and micro-Raman techniques to establish the solubility of Co^{II} in TiO_2 lattice, composition, and microstructure analysis. This investigation demonstrates the successful application of soft chemical route to fabricate ferromagnetic semiconductors with phase purity. Photomediated cobalt(II) dopant implantation into anatase host matrix without significant phase transformation is an encouraging study from the standpoint of the search for new synthesis conditions for ferromagnetic materials.

AUTHOR INFORMATION

Corresponding Author

*E-mail: kanuniv@gmail.com. Tel: +91-413-2654509.

ACKNOWLEDGMENT

K.A. records his sincere thanks to the Department of Science and Technology-Science and Engineering Research Council,

New Delhi and the Council of Scientific and Industrial Research, New Delhi for the financial support. K.A. is extremely thankful to Central Instrumentation Facility, Pondicherry University for providing instrumentation facility and Veeco-India Nanotechnology Laboratory, JNCASIR, Bangalore.

REFERENCES

- (1) (a) Daniel Bryan, J.; Heald, S. M.; Chambers, S. A.; Gamelin, D. R. *J. Am. Chem. Soc.* **2004**, 126, 11640. (b) Fu, N.; Wu, Y.; Jin, Z.; Lu, G. *Langmuir* **2010**, 26, 447.
- (2) (a) Daniel Bryan, J.; Santangelo, S. A.; Keveren, S. C.; Gamelin, D. R. *J. Am. Chem. Soc.* **2005**, 127, 15568. (b) Diamandescu, L.; Vasiliu, F.; Tarabasanu-Mihaila, D.; Feder, M.; Vlaicu, A. M.; Teodorescu, C. M.; Macovei, D.; Enculescu, I.; Parvulescu, V.; Vasile, E. *Mater. Chem. Phys.* **2008**, 112, 146.
- (3) (a) Matsumoto, Y.; Murakami, M.; Shono, T.; Hasegawa, T.; Fukumura, T.; Kawasaki, M.; Ahmet, P.; Chikyow, T.; Koshihara, S.-Y.; Koinuma, H. *Science* **2001**, 291, 854. (b) Manivannan, A.; Glaspell, G.; Dutta, P.; Seehra, M. S. *J. Appl. Phys.* **2005**, 97, 10D325. (c) Manivannan, A.; Seehra, M. S.; Majumder, S. B.; Katiyar, R. S. *Appl. Phys. Lett.* **2003**, 83, 111.
- (4) Kim, H. S.; Gilmer, D. C.; Campbel, S. A.; Polla, D. L. *Appl. Phys. Lett.* **1996**, 69, 3860.
- (5) Fujishima, A.; Honda, K. *Nature* **1972**, 238, 37.
- (6) (a) Barakat, M. A.; Hayes, G.; Ismat Shah, S. J. *Nanosci. Nanotechnol.* **2005**, 5, 759. (b) Shah, S. I.; Unruh, K. M. *Appl. Phys. Lett.* **1991**, 59, 3485.
- (7) (a) Jonker, B. T.; Park, Y. D.; Bennett, B. R.; Cheong, H. D.; Kioseoglou, G.; Petrou, A. *Phys. Rev. B* **2000**, 62, 8180. (b) Fiederling, R.; Kelm, M.; Reuscher, G.; Ossau, W.; Schmidt, G.; Waag, A.; Molenkamp, L. M. *Nature* **1999**, 402, 787.
- (8) (a) Linsebigler, A. L.; Lu, G. Q.; Yates, J. T., Jr. *Chem. Rev.* **1995**, 95, 735. (b) Anbalagan, K.; Stephen, L. D. *Transition Met. Chem.* **2009**, 34, 915.
- (9) (a) Morris Hotsenpiller, P. A.; Bolt, J. D.; Farneth, W. E.; Lowekamp, J. B.; Rohrer, G. S. *J. Phys. Chem. B* **1998**, 102, 3216. (b) Anbalagan, K.; Geethalakshmi, T.; Poonkodi, S. P. R. *J. Phys. Chem. A* **2003**, 107, 1918. (c) Anbalagan, K.; Lydia, I. S. *Spectrochim. Acta, Part A* **2008**, 69, 964. (d) Anbalagan, K.; Stephen, L. D. *Z. Phys. Chem.* **2006**, 220, 335. (e) Xu, A.-W.; Gao, Y.; Liu, H.-Q. *J. Catal.* **2002**, 207, 151.
- (10) Anbalagan, K.; Stephen, L. D. P-92. Presented in the "Photo-radchem 2007, An International Conference on Frontiers of Radiation and Photochemistry, School of Chemical Sciences, Mahatma Gandhi University, Kottayam, Kerala, Feb 8–11, 2007; p 170.
- (11) (a) Marcus, R. A. *J. Phys. Chem.* **1990**, 94, 1050. (b) Poznyak, S. K.; Pergushov, V. I.; Kokorin, A. I.; Kulak, A. I.; Schlaepfer, C. W. *J. Phys. Chem. B* **1999**, 103, 1308.
- (12) Bailar, J. C., Jr.; Clapp, L. B. *J. Am. Chem. Soc.* **1945**, 67, 171.
- (13) Bailar, J. C., Jr.; Rollinson, C. L. *Inorg. Synth.* **1946**, 22, 222.
- (14) Wang, C.-Y.; Liu, C.-Y.; Wang, W.-Q.; Shen, T. J. *Photochem. Photobiol. A* **1997**, 109, 159.
- (15) (a) Asbury, J. B.; Hao, E.; Wang, Y.; Ghosh, H. N.; Lian, T. *J. Phys. Chem. B* **2001**, 105, 4545. (b) Shao, Y.; Chen, W.; Wold, E.; Paul, J. *Langmuir* **1994**, 10, 178.
- (16) Lim, S. H.; Ferraris, C.; Schreyer, M.; Shih, K.; Leckie, J. O.; White, T. J. *J. Solid State Chem.* **2007**, 180, 2905.
- (17) Hagfeldt, A.; Gratzel, M. *Chem. Rev.* **1995**, 95, 49.
- (18) (a) Nozik, A. J.; Memming, R. D. *J. Phys. Chem.* **1996**, 100, 13061. (b) Rajh, T.; Chen, L. X.; Lukas, K.; Liu, T.; Thurnauer, M. C.; Tiede, D. M. *J. Phys. Chem. B* **2002**, 106, 10543.
- (19) Bellardita, M.; Addamo, M.; Di Paola, A.; Palmisano, L. *Chem. Phys.* **2007**, 339, 97.
- (20) (a) Zhou, G.-W.; Lee, D. K.; Kim, Y. H.; Kim, C. W.; Kang, Y. S. *Bull. Korean Chem. Soc.* **2006**, 27, 368. (b) Han, T.-Y.; Wu, C.-F.; Hsieh, C.-T. *J. Vac. Sci. Technol.* **2007**, B25, 430. (c) Karvinen, S. M. *Ind. Eng. Chem. Res.* **2003**, 42, 1035.

- (21) Amadelli, R.; Samiolo, L.; Maldotti, A.; Molinari, A.; Valigi, M.; Gazzoli, D. *Int. J. Photoenergy* **2008**, ID 853753, 1.
- (22) Iwasaki, M.; Hara, M.; Kawada, H.; Tada, H.; Ito, S. *J. Colloid Interface Sci.* **2000**, *224*, 202.
- (23) Pappalardo, R.; Wood, D. L.; Linares, R. C. *J. Chem. Phys.* **1961**, *35*, 2041.
- (24) Verberckmoes, A. A.; Weckhuysen, B. M.; Schoonheydt, R. A. *Microporous Mesoporous Mater.* **1998**, *22*, 165.
- (25) Khaibullin, R. I.; Tagirov, L. R.; Rameev, B. Z.; Ibragimov, Sh. Z.; Yildiz, F.; Aktas, B. *J. Phys.: Condens. Matter.* **2004**, *16*, L443.
- (26) Park, M. S.; Kwon, S. K.; Min, B. I. *Phys. Rev. B.* **2002**, *65*, 161201.
- (27) (a) Das, K.; Sharma, S. N.; Kumar, M.; De, S. K. *J. Phys. Chem. C* **2009**, *113*, 14783. (b) Wang, H.; Branford, W. R.; Cohen, L. F.; Skinner, S. J.; Ryan, M. P. *Chem. Mater.* **2007**, *19*, 3084. (c) Huang, C.; Liu, X.; Liu, Y.; Wang, Y. *Chem. Phys. Lett.* **2006**, *432*, 468. (d) Barakat, M. A.; Schaeffer, H.; Hayes, G.; Ismat-Shah, S. *Appl. Catal., B* **2004**, *57*, 23.
- (28) (a) Glaspell, G.; Manivannan, A. *J. Cluster Sci.* **2005**, *16*, 501. (b) Kuljanin-Jakovljevic, J.; Radoicic, M.; Radetic, T.; Konstantinovic, Z.; Saponjic, Z. V.; Nedeljkovic, J. *J. Phys. Chem. C* **2009**, *113*, 21029.
- (29) Pan, D.; Xu, G.; Wan, J.; Shi, Z.; Han, M.; Wang, G. *Langmuir* **2006**, *22*, 5537.
- (30) Subramanian, M.; Vijayalakshmi, S.; Venkataraj, S.; Jayavel, R. *Thin Solid Films.* **2008**, *516*, 3776.
- (31) Li, J.; Sow, O. H.; Rao, S. X.; Ong, C. K.; Zheng, D. N. *Eur. Phys. J. B* **2003**, *32*, 471.
- (32) Ogale, S.; Kundaliya, D.; Mehraeen, S.; Fu, L.; Zhang, S.; Lussier, A.; Dvorak, J.; Browning, N.; Idzera, Y.; Venketesan, T. *Chem. Mater.* **2008**, *20*, 1344.
- (33) Janisch, R.; Spaldin, N. A. *Phys. Rev. B.* **2006**, *73*, 035201.
- (34) (a) Coey, J. M. D.; Venkatesan, M.; Fitzgerald, C. B. *Nat. Mater.* **2005**, *4*, 173. (b) Jaffe, J. E.; Droubay, T. C.; Chambers, S. A. *J. Appl. Phys.* **2005**, *97*, 073908.
- (35) Sullivan, J. M.; Erwin, S. C. *Phys. Rev. B.* **2003**, *67*, 144415.
- (36) (a) Anderson, P. W. *Phys. Rev.* **1950**, *79*, 350. (b) Goodenough, J. B. *Phys. Rev.* **1955**, *100*, 564. (c) Kanamori, J. *J. Phys. Chem. Solids.* **1959**, *10*, 87.
- (37) (a) Geng, W. T.; Kim, K. S. *Solid. State. Commun.* **2004**, *129*, 741. (b) Geng, W. T.; Kim, K. S. *Phys. Rev. B.* **2003**, *68*, 125203.
- (38) Weng, H.; Yang, X.; Dong, J.; Mizuseki, H.; Kawasaki, M.; Kawazoe, Y. *Phys. Rev. B.* **2004**, *69*, 125219.
- (39) (a) Tachikawa, T.; Choi, J. R.; Fujitsuka, M.; Majima, T. *J. Phys. Chem. C* **2008**, *112*, 14090. (b) Griffin, K. A.; Pakhomov, A. B.; Wang, C. M.; Heald, S. M.; Krishnan, K. M. *Phys. Rev. Lett.* **2005**, *94*, 157204. (c) Griffin, K. A.; Pakhomov, A. B.; Wang, C. M.; Heald, S. M.; Krishnan, K. M. *Phys. Rev. Lett.* **2005**, *94*, 173.
- (40) Lisong, Y.; Qifa, Z.; Xingui, T. *Chin. Funct. Mater.* **1999**, *30*, 498.
- (41) Sanjines, R.; Tang, H.; Berger, H.; Gozzo, F.; Margaritondo, G.; Levy, F. *J. Appl. Phys.* **1994**, *75*, 2945.
- (42) (a) Watanabe, M.; Hayashi, T. *J. Lumin.* **2005**, *112*, 88. (b) Sildos, I.; Suisalu, A.; Aarik, J.; Sekiya, T.; Kurita, S. *J. Lumin.* **2000**, *87*, 290.
- (43) Lei, Y.; Zhang, L. D.; Meng, G. W.; Li, G. H.; Zhang, X. Y.; Liang, C. H.; Chen, W.; Wang, S. X. *Appl. Phys. Lett.* **2001**, *78*, 1125.
- (44) Losev, N.; Smagunova, A. *The Principles of X-ray Fluorescence Analysis*; Khimia: Moscow, 1982; p 207 (in Russian).
- (45) (a) Djerdj, I.; Arcon, D.; Jaglicic, Z.; Niederberger, M. *J. Solid State Chem.* **2008**, *181*, 1571. (b) Panneer Muthuselvam, I.; Poddar, A.; Bhowmik, R. N. *J. Alloys Compd.* **2009**, *486*, 536.
- (46) Park, S.; DiMasi, E.; Kim, Y.-I.; Han, W.; Woodward, P. M.; Vogt, T. *Thin Solid Films* **2006**, *515*, 1250.
- (47) (a) Moulder, J. F.; Stickle, W. F.; Sobol, P. E.; Bomben, K. D. *Handbook of X-Ray Photoelectron Spectroscopy*; Perkin-Elmer: Eden Prairie, MN, 1992. (b) Vob, M.; Borgmann, D.; Wedler, G. *J. Catal.* **2002**, *212*, 10. (c) Orendor, A.; Wusten, J.; Ziegler, C.; Gnaser, H. *Appl. Surf. Sci.* **2005**, *252*, 85. (d) Gopel, W.; Anderson, J. A.; Frankel, D.; Jaehning, M.; Phillips, K.; Schafer, J. A.; Rocker, G. *Surf. Sci.* **1984**, *139*, 333. (e) Manivannan, A.; Majumder, S. B.; Katiyar, R. S. *Mater. Res. Soc. Symp. Proc.* **2002**, *15*, 5.
- (48) Lin, Y.-H.; Zhang, S.; Deng, C.; Zhang, Y.; Wang, X.; Nan, C.-W. *Appl. Phys. Lett.* **2008**, *92*, 112501.
- (49) (a) Towle, S. N.; Bargar, J. R.; Brown, G. E., Jr.; Parks, G. A. *J. Col. Inter. Sci.* **1997**, *187*, 62. (b) Song, H.-Q.; Mei, L.-M.; Yan, S.-S.; Ma, X.-L.; Liu, J. P.; Wang, Y.; Zhang, Z. *J. Appl. Phys.* **2006**, *99*, 123903.
- (50) Jeong, B.-S.; Heo, Y. W.; Norton, D. P.; Kelly, J. G.; Rairigh, R.; Hebard, A. F.; Budai, J. D.; Park, Y. D. *Appl. Phys. Lett.* **2004**, *84*, 2608.
- (51) Anisimov, V. I.; Korotin, M. A.; Nekrasov, I. A.; Mylnikova, A. S.; Lukoyanov, A. V.; Wang, J. L.; Zeng, Z. *J. Phys.: Condens. Matter.* **2006**, *18*, 1695.
- (52) Jongsomjit, B.; Sakdarnuson, C.; Goodwin, J. G., Jr.; Prasertthadam, P. *Cat. Lett.* **2004**, *94*, 209.
- (53) Lottici, P. P.; Bersani, D.; Braghini, M.; Montenero, A. *J. Mater. Sci.* **1993**, *28*, 177.
- (54) Whang, C. M.; Kim, J. G.; Kim, E. Y.; Kim, Y. H.; Lee, W. I. *Glass. Phys. Chem.* **2005**, *31*, 390.
- (55) Chong, S. V.; Xia, J.; Suresh, N.; Yamaki, K.; Kadowaki, K. *Solid State Commun.* **2008**, *148*, 345.
- (56) Huang, C.; Liu, X.; Kong, L.; Lan, W.; Su, Q.; Wang, Y. *Appl. Phys. A: Mater. Sci. Process.* **2007**, *87*, 781.
- (57) Gole, J. L.; Prokes, S. M.; White, M. G. *Appl. Surf. Sci.* **2008**, *255*, 718.
- (58) Camacho-Lopez, M. A.; Vargas, S.; Arroyo, R.; Haro-Poniatowski, E.; Rodriguez, R. *Optical Mater.* **2002**, *20*, 43.
- (59) Bersani, D.; Lottici, P. P.; Ding, X.-Z. *Appl. Phys. Lett.* **1998**, *72*, 73.
- (60) Parker, J. C.; Siegel, R. W. *Appl. Phys. Lett.* **1990**, *57*, 943.